



**HAL**  
open science

# **Nanocellulose-derived carbon/g-C<sub>3</sub>N<sub>4</sub> heterojunction with a hybrid electron transfer pathway for highly photocatalytic hydrogen peroxide production**

Yiwei Shan, Ying Guo, Yu Wang, Xiran Du, Jun Yu, Hao Luo, Hui Wu, Bruno Boury, He Xiao, Liulian Huang, et al.

## **► To cite this version:**

Yiwei Shan, Ying Guo, Yu Wang, Xiran Du, Jun Yu, et al.. Nanocellulose-derived carbon/g-C<sub>3</sub>N<sub>4</sub> heterojunction with a hybrid electron transfer pathway for highly photocatalytic hydrogen peroxide production. *Journal of Colloid and Interface Science*, 2021, 599, pp.507-518. <10.1016/j.jcis.2021.04.111>. <hal-03276337>

**HAL Id: hal-03276337**

**<https://hal.umontpellier.fr/hal-03276337v1>**

Submitted on 9 May 2023

**HAL** is a multi-disciplinary open access archive for the deposit and dissemination of scientific research documents, whether they are published or not. The documents may come from teaching and research institutions in France or abroad, or from public or private research centers.

L'archive ouverte pluridisciplinaire **HAL**, est destinée au dépôt et à la diffusion de documents scientifiques de niveau recherche, publiés ou non, émanant des établissements d'enseignement et de recherche français ou étrangers, des laboratoires publics ou privés.



Distributed under a Creative Commons CC BY-NC 4.0 - Attribution - Non-commercial use - International License

1        **Nanocellulose-derived carbon/g-C<sub>3</sub>N<sub>4</sub> heterojunction with a**  
2        **hybrid electron transfer pathway for highly photocatalytic**  
3        **hydrogen peroxide production**

4  
5        Yiwei Shan <sup>a</sup>, Ying Guo <sup>a</sup>, Yu Wang <sup>a</sup>, Xiran Du <sup>a</sup>, Jun Yu <sup>a</sup>, Hao Luo <sup>a</sup>, Hui Wu <sup>a</sup>,  
6        Bruno Boury <sup>b,\*</sup>, He Xiao <sup>a,\*</sup>, Liulian Huang <sup>a</sup>, Lihui Chen <sup>a</sup>

7  
8        <sup>a</sup> College of Material Engineering, Fujian Agriculture and Forestry University, Fuzhou, 350108,  
9        China

10       <sup>b</sup> ICGM, University of Montpellier, CNRS, ENSCM, Montpellier, France

11  
12       Corresponding authors: Bruno Boury (bruno.boury@umontpellier.fr),

13       He Xiao (xiaohe\_river@163.com)

14  
15       **Abstract**

16       Using oxygen reduction for the photocatalytic production of hydrogen peroxide (H<sub>2</sub>O<sub>2</sub>)  
17       has been considered a green and sustainable route. In the present study, to achieve  
18       high efficiency, graphitic carbon nitride (g-C<sub>3</sub>N<sub>4</sub>) was obtained using thermal  
19       polymerization from a bi-component precursor and was then assembled with cellulose  
20       nanofibers. It was found that a small quantity of cellulose nanofibers that generates  
21       carbon fibers upon pyrolysis greatly improves the photocatalytic activity compared  
22       with that of g-C<sub>3</sub>N<sub>4</sub> alone. The well-defined carbon/g-C<sub>3</sub>N<sub>4</sub> heterojunction-type  
23       material exhibits as high as 1.10 mmol L<sup>-1</sup> h<sup>-1</sup> of photo-production of H<sub>2</sub>O<sub>2</sub> under  
24       visible light, which is 4.2 times higher than that yielded by pristine g-C<sub>3</sub>N<sub>4</sub> from a  
25       single precursor. A comprehensive characterization of the photocatalyst enables us to  
26       delineate the effect of the carbon nanofiber with respect to porosity, electron–hole  
27       separation, band gap regulation, and especially the electron transfer pathway. Our

28 results demonstrate that nanocellulose-derived carbon, when precisely assembled with  
29 other functional material such as a photocatalyst, is a promising promoter of their  
30 activity.

31

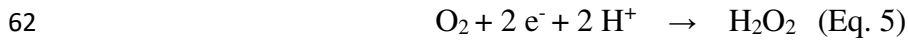
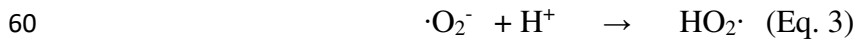
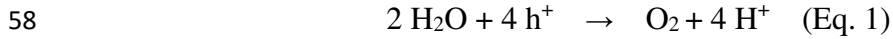
32 **Keywords:** Cellulose nanofibers; Photocatalysis; Carbon nitride; Hydrogen peroxide  
33 production; Carbon fibers

34

## 35 1. Introduction

36 Hydrogen peroxide ( $\text{H}_2\text{O}_2$ ) is a promising energy storage product widely used  
37 both as an oxidant and reductant in chemical synthesis, industrial bleaching, and  
38 medical sterilization [1, 2]. Moreover, in line with the need for new answers to the  
39 increase in energy demand,  $\text{H}_2\text{O}_2$  has been proposed as the oxidizing agent at the  
40 cathode of fuel cells with environmentally acceptable by-products,  $\text{H}_2\text{O}$  and  $\text{O}_2$  [3].  
41 Presently, the methods adopted to produce  $\text{H}_2\text{O}_2$  on a large scale are anthraquinone  
42 autoxidation [4] and electrochemical synthesis [5]. These methods consume a large  
43 amount of energy and organic solvents; in addition, contamination by various organic  
44 impurities can occur and result in increased difficulties of purification [6, 7].  
45 Consequently, new production processes must succeed in satisfying the demand for  
46  $\text{H}_2\text{O}_2$ , resolve and eliminate the shortcomings of traditional production methods, be  
47 efficient, and above all be sustainable and environmentally friendly with respect to the  
48 principles of green chemistry.

49 In recent decades, photocatalysis has been employed in light-driven production  
50 of  $\text{H}_2\text{O}_2$  through photoreduction of  $\text{O}_2$  in  $\text{H}_2\text{O}$  [8], a process governed by the basic  
51 photochemical reaction resulting from light–semiconductor interaction in the presence  
52 of water. In this approach, the semiconductor generates holes ( $\text{h}^+$ ) in the valence band  
53 (VB) that oxidize  $\text{H}_2\text{O}$  near the surface and release protons ( $\text{H}^+$ ; Eq. 1).  
54 Simultaneously, the electrons ( $\text{e}^-$ ) promoted in the conduction band (CB) can reduce  
55  $\text{O}_2$  to generate different species, including superoxide radicals ( $\cdot\text{O}_2^-$ ) and, subsequently,  
56  $\text{H}_2\text{O}_2$  by either a (i) single-electron indirect reduction and protonation (Eq. 2–4) or (ii)  
57 one-step two-electron direct  $\text{O}_2$  reduction (Eq. 5).



63 ZnO [9] and TiO<sub>2</sub> [10-14] are the two major classical inorganic semiconductors  
64 used as photocatalysts [15, 16], among many others. Recently, carbon nitride with  
65 graphitic structure (g-C<sub>3</sub>N<sub>4</sub>) has emerged as a highly promising photocatalyst.  
66 Compared with classical metal-based semiconductors, it has a high efficiency and  
67 several advantages [17-20], the most attractive one being the absence of metal species  
68 known to decompose H<sub>2</sub>O<sub>2</sub> via MOOH formation. Additionally, g-C<sub>3</sub>N<sub>4</sub>-based  
69 catalysts exhibit good photostability and photocatalytic activity under visible light.  
70 Finally, g-C<sub>3</sub>N<sub>4</sub> can be prepared by the polycondensation and pyrolysis (500–600°C)  
71 of nitrogen- and carbon-containing precursors such as melamine and urea, both being  
72 cheap, abundant, and non-toxic in comparison with ZnO and TiO<sub>2</sub> [21]. However,  
73 pure carbon nitride has some bottlenecks limiting its photocatalytic efficiency, such as  
74 a fast electron–hole recombination of photogenerated species, insufficient absorption  
75 in visible light, a relatively large band gap (~2.7 eV), and a low specific surface area  
76 that limits the number of active sites for interfacial photoreactions. To address these  
77 issues, different strategies have been employed to enhance the photocatalytic activity,  
78 including non-metal doping (e.g., O [22, 23], P [24], N [25], and S [26]), metal ion  
79 doping (K [7], Cu [27]), forming heterojunctions with other semiconductors (e.g.,  
80 ZnO [28], MnO<sub>2</sub> [29], and CeO<sub>2</sub> [30]), composites with metal nanoparticles (e.g., Au  
81 [20] and Ag [31]), and composites with carbonaceous materials (e.g., carbon dots [32],  
82 graphene [33], and carbon nanotubes [34]). The carbonaceous materials are selected  
83 as an electron transfer agent and photosensitizer in the photocatalysis field to reduce  
84 the electron–hole (e<sup>-</sup>/h<sup>+</sup>) recombination and to increase the absorption of incident light,  
85 respectively. Nowadays, the production of such functional carbon should avoid the  
86 use of non-renewable and fossil fuel-derived carbon precursors (e.g., polyacrylonitrile  
87 [PAN]), and instead use biosourced carbon. Cellulose nanofibers (CNF) are one

88 example, with 1–3  $\mu\text{m}$  length and 5–10 nm width. They not only have the advantage  
89 of size but also possess adequate surface functional groups such as -OH and -COOH,  
90 facilitating regulation of the growth and chemical anchoring of chemical species such  
91 as precursors of inorganic photocatalysts [35]. Therefore, anchoring graphitic-like  
92 materials should be possible if they possess compatible functional groups. This  
93 implies the necessity of edge functional groups in g-C<sub>3</sub>N<sub>4</sub> that possess H-bonding  
94 donor or acceptor ability.

95 Various research groups have already demonstrated the synergy of  
96 nanocellulose/g-C<sub>3</sub>N<sub>4</sub> composites, with or without pyrolysis of the cellulose. It has led  
97 to the development of adsorbents or photocatalysts for the oxidation of dyes  
98 (methylene blue [36-39] or rhodamine [40, 41]), formaldehyde [42], Cr(IV) [43, 44],  
99 oil/water emulsion [45] or bacteria [46] and also the preparation of thermal insulator  
100 materials [47, 48]. These are promising routes especially for pollutant remediation;  
101 however, the future of photocatalysis also involves the production of chemicals by  
102 clean and low-energy processes. To the best of our knowledge, only one previous  
103 study used g-C<sub>3</sub>N<sub>4</sub> and nanocellulose to produce an efficient photocatalyst to produce  
104 chemicals, H<sub>2</sub> in that case. However, nanocellulose was used only as a template to  
105 generate a chiral nematic structure in addition to the use of silica, with nanocellulose  
106 subsequently eliminated by calcination [49]. In our study, we used nanocellulose as  
107 both a template and a C-precursor to prepare a C/g-C<sub>3</sub>N<sub>4</sub> composite by the simplest  
108 possible process. It is also worth mentioning the work by Jin et al., who used soluble  
109 cellulose acetate in combination with melamine as a g-C<sub>3</sub>N<sub>4</sub> precursor to produce a  
110 C/g-C<sub>3</sub>N<sub>4</sub> photocatalyst for the production of hydrogen [50].

111 In the present study, g-C<sub>3</sub>N<sub>4</sub> nanosheets (CN2) were fabricated for the first time  
112 using a mixture of melamine and urea and a two-step calcination method, to generate  
113 a higher proportion of amino groups (-NH<sub>x</sub>) than that in g-C<sub>3</sub>N<sub>4</sub> prepared with only  
114 melamine (CN1); see Scheme 1 for the summary of the general strategy. We found  
115 that the as-prepared g-C<sub>3</sub>N<sub>4</sub> nanosheets can easily and strongly bind the CNF, possibly  
116 by hydrogen or even covalent bonds. The cellulose nanofiber/g-C<sub>3</sub>N<sub>4</sub> composite is  
117 then transformed by pyrolysis into a covalent heterojunction C/g-C<sub>3</sub>N<sub>4</sub> (CNCF1 or

118 CNCF2) with consequences on the band structure and electron transfer process and an  
119 important improvement in the photocatalytic activity. As usual when designing a  
120 nanocomposite, apart from the nature of the interaction between the components, their  
121 mass ratio is an important factor. Prior experiments demonstrated that the optimum  
122 mass ratio of the cellulose nanofiber/g-C<sub>3</sub>N<sub>4</sub> is ~3–4 %; therefore, this ratio was  
123 implemented throughout this study.

124

## 125 **2. Experimental**

### 126 *2.1 Materials and reagents*

127 Melamine (C<sub>3</sub>H<sub>6</sub>N<sub>6</sub>; 99%), urea (CH<sub>4</sub>N<sub>2</sub>O; 99.5%), potassium dihydrogen  
128 phosphate (KH<sub>2</sub>PO<sub>4</sub>; 99.5%), potassium hydrogen phosphate (K<sub>2</sub>HPO<sub>4</sub>; 99%),  
129 N,N-Diethyl-p-phenylenediamine sulfate (DPD; 98%), horseradish peroxidase (POD;  
130 enzymatic activity >160 units/mg), anhydrous ethanol (AR), 5,5-dimethyl-1-pyrroline  
131 N-oxide (DMPO, 97%) were obtained from Aladdin Industrial Co., Ltd, China.  
132 Cellulose nanofibers (1 wt% aqueous solution; average length: 1–3 μm, average width:  
133 5–10 nm) was purchased from Guilin Qihong Technology Co., Ltd., China.  
134 Polyethersulfone (PES) membrane (Ø 13 mm × 0.22 μm) was obtained from Jin Teng  
135 Experimental Equipment Co., Ltd., Tianjin, China. All the chemical reagents  
136 mentioned above were of analytical grade and were utilized without further  
137 purification.

138

### 139 *2.2 Preparation of photocatalysts*

140 The g-C<sub>3</sub>N<sub>4</sub> nanosheets were synthesized by a two-step pyrolysis treatment of  
141 melamine and urea [51]. First, melamine (3.2 g) and urea (0.8 g) were uniformly  
142 mixed and thoroughly ground in an agate mortar. The samples were placed into a  
143 muffle furnace and heated to 500°C with a heating rate of 2°C min<sup>-1</sup> in static air and  
144 left for 2 h; then, the temperature was risen to 520°C for 2 h at the heating rate of 2°C  
145 min<sup>-1</sup>. The residual yellow solids were ground into powder and calcined at 520°C for  
146 4.5 h in air. Finally, the resultant light-yellow products with a productivity of 30%  
147 were denoted as CN2. For comparison, g-C<sub>3</sub>N<sub>4</sub> nanosheets from a single precursor

148 was also synthesized by calcining pure melamine through the same thermal treatment  
149 and denoted as CN1, with a productivity of 36%.

150 The g-C<sub>3</sub>N<sub>4</sub> composited with nanocarbon fibers was prepared by a one-step  
151 thermal treatment of the compound of g-C<sub>3</sub>N<sub>4</sub> and CNF. In brief, g-C<sub>3</sub>N<sub>4</sub> nanosheets  
152 (CN1 or CN2; 0.10 g) was added into 10 mL of deionized water containing a  
153 suspension of CNF (0.33 g; CNF concentration 1 wt%) and ultrasonicated for 30 min,  
154 as shown in Figure S1. Subsequently, the mixtures were vacuum-dried at 60°C for 12  
155 h. Then, the residual white yellow solids were directly pyrolyzed at 500°C for 1 h at  
156 the heating rate of 5°C min<sup>-1</sup> in argon atmosphere, marked as CNCF<sub>x</sub> (x = 1, 2). The  
157 final products (CNCF1 and CNCF2) obtained also retained the productivity of 80%  
158 and 70%, respectively. The pure CNF were carbonized into cellulosic carbon fibers,  
159 denoted as CF, under the same calcination conditions.

160

### 161 2.3 Characterization

162 The crystal structures of as-prepared samples were characterized using an X-ray  
163 diffractometer (Rigaku, Ultima IV, Japan) with Cu K $\alpha$  radiation in the range between  
164 5° and 80°. Fourier transform infrared (FTIR) spectra were recorded on a Bruker  
165 VERTEX 70 spectrophotometer at the wavelength ranging from 400 to 4000 cm<sup>-1</sup>.  
166 The porosimetry measurements and BET-specific surface area of the samples was  
167 detected by nitrogen adsorption/desorption on an adsorption apparatus (Micromeritics,  
168 ASAP 2020, USA). The morphologies of the samples were observed using a scanning  
169 electron microscope (Hitachi, SU8010, Japan) and transmission electron microscope  
170 (JEOL, JEM-2100, Japan). The X-ray photoelectron spectrometer (XPS, ESCALAB  
171 250, Thermo Scientific, USA) equipped with Al K $\alpha$  radiation monochromatic source  
172 was used to detect chemical composition and elemental states. The ultraviolet  
173 (UV)-vis diffuse reflectance spectra (UV-vis DRS) were obtained using a UV-vis  
174 spectrophotometer (Cary 500, Varian, USA) in the range of 300–800 nm with BaSO<sub>4</sub>  
175 as a reflectance standard. Photoluminescence spectra were recorded on a LS55  
176 spectrophotometer (Perkin-Elmer, USA) under the excitation wavelength of 365 nm at  
177 room temperature. Time-resolved photoluminescence (TRPL) spectra were obtained  
178 on a fluorescence spectrophotometer (FLS980, Edinburgh Instruments, UK).  
179 Photo-generated ·O<sub>2</sub><sup>-</sup> radical species in the photocatalytic process were detected with  
180 DMPO as a trapping agent. The absorbance of hydrogen peroxide solution was

181 determined by UV–visible spectrophotometer (US-Vis, Agilent 8453, USA) at the  
182 wavelength 551 nm.

#### 183 *2.4 Photoelectrochemical and electrochemical measurement*

184 The transient photocurrent curves and electrochemical impedance spectroscopy  
185 were obtained on CHI660-E electrochemical workstation (Chenhua Instrument  
186 Company, Shanghai, China) based on a three-electrode cell composed of Pt wire as  
187 the counter electrode, Ag/AgCl electrode as the reference electrode, and  
188 fluorine-doped tin oxide (FTO) glass ( $1 \times 1 \text{ cm}^2$ ) as the working electrode.  $\text{Na}_2\text{SO}_4$   
189 aqueous solution (0.2 mol/L) was used as the electrolyte. Five milligrams of the  
190 sample (CNx or CNCFx) was added to 1 mL of Nafion solution (0.5%) under  
191 ultrasonication for 30 min, and then deposited onto the FTO glass. The as-prepared  
192 working electrode was dried at  $80^\circ\text{C}$  for 3 h. The photoelectrochemical measurement  
193 was performed under visible light irradiation (Xe arc lamp: 300 W, the distance  
194 between the surface of the solution and light filter: 10 cm, filter wavelength:  $\lambda > 420$   
195 nm). The transient photocurrent was collected with the light on and off. The  
196 electrochemical impedance spectroscopy (EIS) was tested at the frequency of 0.01  
197 and  $10^6$  Hz with the alternating current amplitude of 5 mV.

198 Rotating disk electrode (RDE) tests were also taken on a CHI660-E  
199 electrochemical workstation with a modulated speed rotator and a glassy carbon disk  
200 electrode (working electrode). The Ag/AgCl electrode and Pt wire electrode were  
201 used as the reference electrode and counter electrode, respectively. Two milligrams of  
202 the photocatalyst was dispersed into 1 mL of Nafion solution (10%) under  
203 ultrasonication for 30 min. Then, 10  $\mu\text{L}$  of the suspension was dropped on a glassy  
204 carbon electrode with a diameter of 5 mm and air-dried at room temperature as the  
205 working electrode. The linear sweep voltammetry (LSV) curves were obtained using a  
206 phosphate buffer solution (0.1 mmol/L; pH 7) with  $\text{O}_2$ -saturated purging at a scanning  
207 rate of 10 mV/s and the rotating speed between 0 and 2500 rpm.

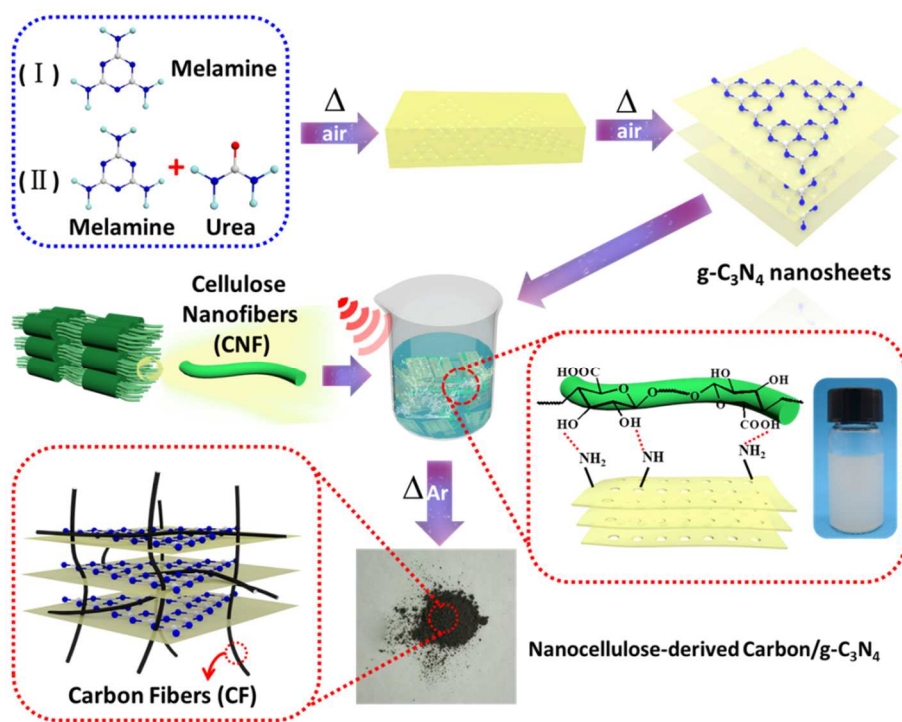
208

#### 209 *2.5 Photocatalytic activity measurements*

210 For evaluating the photocatalytic  $\text{H}_2\text{O}_2$  generation, the catalyst powder (50 mg)  
211 was dispersed in a solution of deionized water (45 mL) and ethanol (5 mL). Then, the  
212 suspension was ultrasonicated for 5 min and purged with  $\text{O}_2$  gas for 30 min prior to  
213 visible irradiation. Then, the photocatalytic performance was examined under visible

214 light irradiation (Xe arc lamp: 300 W, the distance between surface of the solution and  
215 light filter: 10 cm, filter wavelength:  $\lambda > 420$  nm) with continuous O<sub>2</sub> purging and  
216 stirring for 6 h. Every hour, an aliquot of the suspension (4 mL) was taken and filtered  
217 to remove the catalysts. The concentration of H<sub>2</sub>O<sub>2</sub> was measured by a colorimetric  
218 method. To this end, 5 mL of the filtered solution was immediately mixed with 0.5  
219 mL of phosphate buffer (0.5 M K<sub>2</sub>HPO<sub>4</sub> and 0.5 M KH<sub>2</sub>PO<sub>4</sub>), DPD solution (50  $\mu$ L),  
220 and peroxidase (50  $\mu$ L), with vigorous shaking for 30 s. Then, the absorbance of the  
221 aqueous solution was measured at 551 nm using a UV-visible spectrophotometer  
222 [52].

223 The decomposition behavior of H<sub>2</sub>O<sub>2</sub> with photocatalysts was investigated by  
224 adding 50 mg of the samples to 50 mL of H<sub>2</sub>O<sub>2</sub> solution (1 mmol/L) with continuous  
225 stirring under visible light irradiation for 1 h. The stability of the as-prepared samples  
226 was evaluated by performing three consecutive tests. When finishing each run, the  
227 photocatalyst was collected using membrane filtration and washed with deionized  
228 water, then vacuum-dried at 50°C overnight, finally reused in the next cycle under the  
229 same conditions. Photocatalytic H<sub>2</sub>O<sub>2</sub> concentration was also investigated by  
230 measuring the absorbance of the filtrate according to the Beer-Lambert law [52].



231

232

Scheme 1. Procedures for sample synthesis

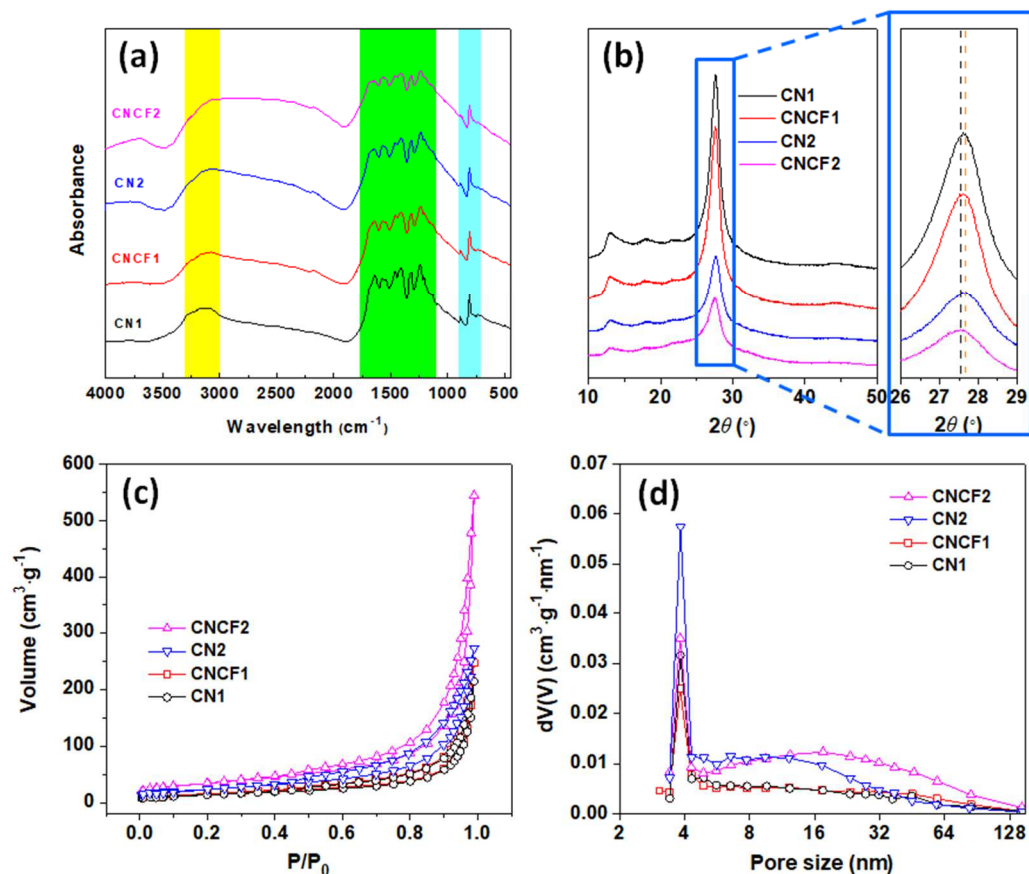
233

### 234 **3. Results and discussion**

#### 235 **3.1 Photocatalyst preparation and characterization**

236 Specific surface area is important for the activity of a photocatalyst; therefore, a  
237 bi-component approach was selected to prepare g-C<sub>3</sub>N<sub>4</sub> with the highest possible  
238 surface area [53, 54]. Urea was used as an additive to melamine owing to the release  
239 of large quantities of volatile gas during thermal treatment, resulting in high porosity  
240 [55, 56]. It also can generate a high quantity of residual amino groups, generally on  
241 the edges of the nanosheets. Because CNF have surface -OH and -COOH groups,  
242 H-bonding and formation of amide or ester groups can occur through reactions with  
243 amino-rich carbon nitride. For comparison, a g-C<sub>3</sub>N<sub>4</sub> was prepared by the  
244 mono-component approach using only melamine, which is referred to as CN1. A  
245 comparison between the dispersal behaviors of CN1 and CN2 with CNF in aqueous  
246 phase is shown in Figure S1, suggesting a higher stabilization of the suspension in the  
247 case of CNF/CN2 mixture.

248 Carbonization at 500°C of the CNF/CN1 and CNF/CN2 mixtures transforms  
249 their CNF into carbon, generating porosity throughout the materials and modifying  
250 the hydrophilic/hydrophobic balance of the surface in the corresponding CNCF1 and  
251 CNCF2, as shown in Figure S2. The results show that the CN2 (from dual precursors)  
252 was more hydrophilic than CN1 (from single precursor) owing to the presence of  
253 more hydrophilic groups (amino groups) in CN2. Moreover, the contact angles of  
254 CN1 (24.5°) and CN2 (20.5°) respectively decreased to 17.6° (CNCF1) and 11°  
255 (CNCF2) when g-C<sub>3</sub>N<sub>4</sub> assembled with the carbon nanofibers pyrolyzed from  
256 nanocellulose was used, because of the increase in the stacking distance in g-C<sub>3</sub>N<sub>4</sub>.  
257 The optimized mass ratio of CNF/g-C<sub>3</sub>N<sub>4</sub> is ~3.3 wt%, which is a miniscule quantity  
258 of CNF, but as shown below, it has a substantial effect on the photocatalytic  
259 performance compared with pure carbon nitride. Moreover, the sample yield is ~70–  
260 80% and with cheap and renewable products. This weight loss is attributed to the  
261 decomposition of cellulose and also the condensation reaction between the surface  
262 functional groups of cellulose and g-C<sub>3</sub>N<sub>4</sub>.



263

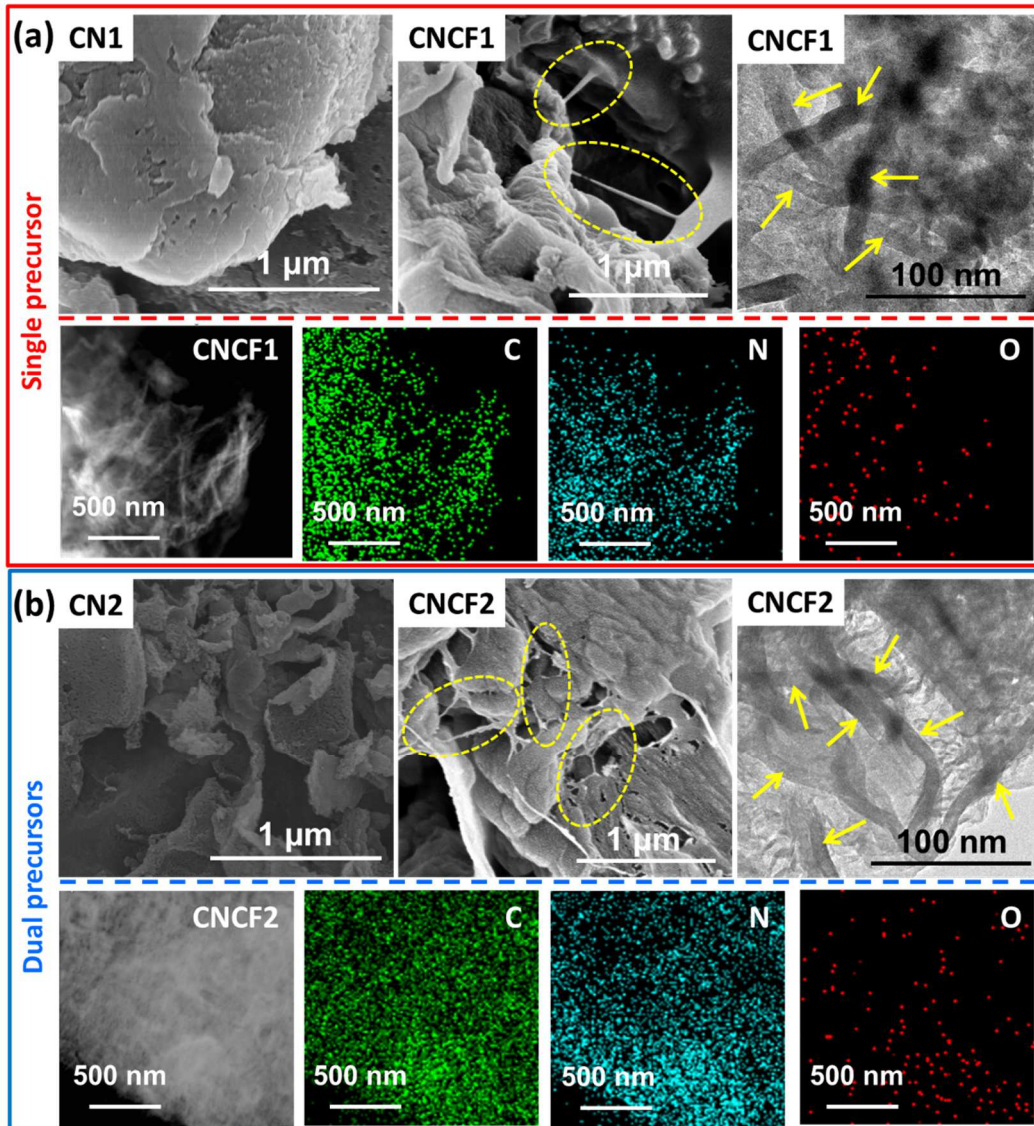
264 **Figure 1.** Fourier transform infrared spectroscopy curves (a), X-ray diffraction patterns (b),  $N_2$   
 265 adsorption-desorption isotherms (c) and pore size distribution derived from desorption isotherm (d)  
 266 of CN1, CN2, CNCF1, and CNCF2.

267

268 The generation of carbon results in an important modification of the color of the  
 269 material from slightly yellow for pure carbon nitride (CN1 and CN2) to gray for  
 270 CNCF1 and CNCF2, as shown in Figure S3. Analyzed by FT-IR (Figure 1a), all  
 271 spectra of  $CN_x$  and  $CNCF_x$  ( $x = 1, 2$ ) are dominated by the signals related to the  
 272 presence of  $g-C_3N_4$ . Several strong bands in the  $1200\text{--}1600\text{ cm}^{-1}$  region were typical  
 273 for the stretching modes of the CN heterocycles [57]. The sharp peak at  $810\text{ cm}^{-1}$   
 274 corresponds to the characteristic breathing vibration of tri-s-triazine units [58]. The  
 275 broad bands ranging from  $3000\text{ cm}^{-1}$  to  $3300\text{ cm}^{-1}$  correspond to the NH and OH  
 276 stretching vibrations [59]. The peak intensity of  $-NH_x$  between  $3000\text{ cm}^{-1}$  and  $3300$   
 277  $\text{cm}^{-1}$  in CNCF1 and CNCF2 is slightly lower than that of CN1 and CN2, respectively;  
 278 it implies a decrease in the number of amino groups [60].

279 The presence of g-C<sub>3</sub>N<sub>4</sub> was also clearly detected in the signals observed in the  
280 X-ray diffraction powder patterns of the CN<sub>x</sub> and CNCF<sub>x</sub> samples, as shown in  
281 Figure 1b. The two characteristic peaks at  $2\theta = 12.9^\circ$  and  $27.5^\circ$  are ascribed to the  
282 (100) and (002) diffraction planes of the in-plane repeat tri-s-triazine units and the  
283 interlayer stacking reflection of conjugated aromatic segments, respectively [61-63].  
284 A slight downshift in the position of the (002) crystal plane was detected when  
285 comparing CN1 and CN2 and CNCF<sub>x</sub>. It corresponds to a very small increase in the  
286 stacking distance in g-C<sub>3</sub>N<sub>4</sub> when assembled with the carbon nanofibers [64], possibly  
287 owing to the intercalation of organic species during pyrolysis. A weaker peak intensity  
288 of (002) was noted for CN2 and CNCF2 than for CN1 and CNCF1, respectively,  
289 which may be ascribed to the effective exfoliation of g-C<sub>3</sub>N<sub>4</sub> into sheet-like structures  
290 by overcoming the weak van der Waals forces between layers in the calcination  
291 process; this finding is consistent with other reports on g-C<sub>3</sub>N<sub>4</sub> [65].

292 Porosity of the materials was determined by N<sub>2</sub> adsorption-desorption with the  
293 isotherms shown in Figure 1c. All samples exhibited typical type IV isotherms with  
294 H3 type hysteresis loops, indicating that the samples were micro-, meso-, and slightly  
295 macroporous with a specific surface area of 50 m<sup>2</sup> g<sup>-1</sup> (CN1), 55 m<sup>2</sup> g<sup>-1</sup> (CNCF1), 83  
296 m<sup>2</sup> g<sup>-1</sup> (CN2), and 120 m<sup>2</sup> g<sup>-1</sup> (CNCF2). The data emphasize the effect of CNF in  
297 addition to the preparation method of g-C<sub>3</sub>N<sub>4</sub>. CN2 and CNCF2 exhibited 1.5–2.4  
298 times higher BET SSA than CN1 and CNCF1 (Table S1). An increase was also  
299 observed for the average pore volume, calculated to be 0.34 m<sup>3</sup> g<sup>-1</sup> (CN1), 0.39 m<sup>3</sup> g<sup>-1</sup>  
300 (CNCF1), 0.44 m<sup>3</sup> g<sup>-1</sup> (CN2), and 0.85 m<sup>3</sup> g<sup>-1</sup> (CNCF2; Table S1). Clearly, the  
301 bi-component route results in materials with enhanced porosity that is ascribed to a  
302 higher proportion of CO<sub>2</sub> and NH<sub>3</sub> release during calcination [66]. Notably, the  
303 assembly of CNF with CN1 or CN2 leads to a decrease in the number of small  
304 mesopores and an increase in the number of large mesopores increased, which is  
305 expected when considering the formation of carbonaceous residue upon pyrolysis of  
306 CNF (Figure 1d).



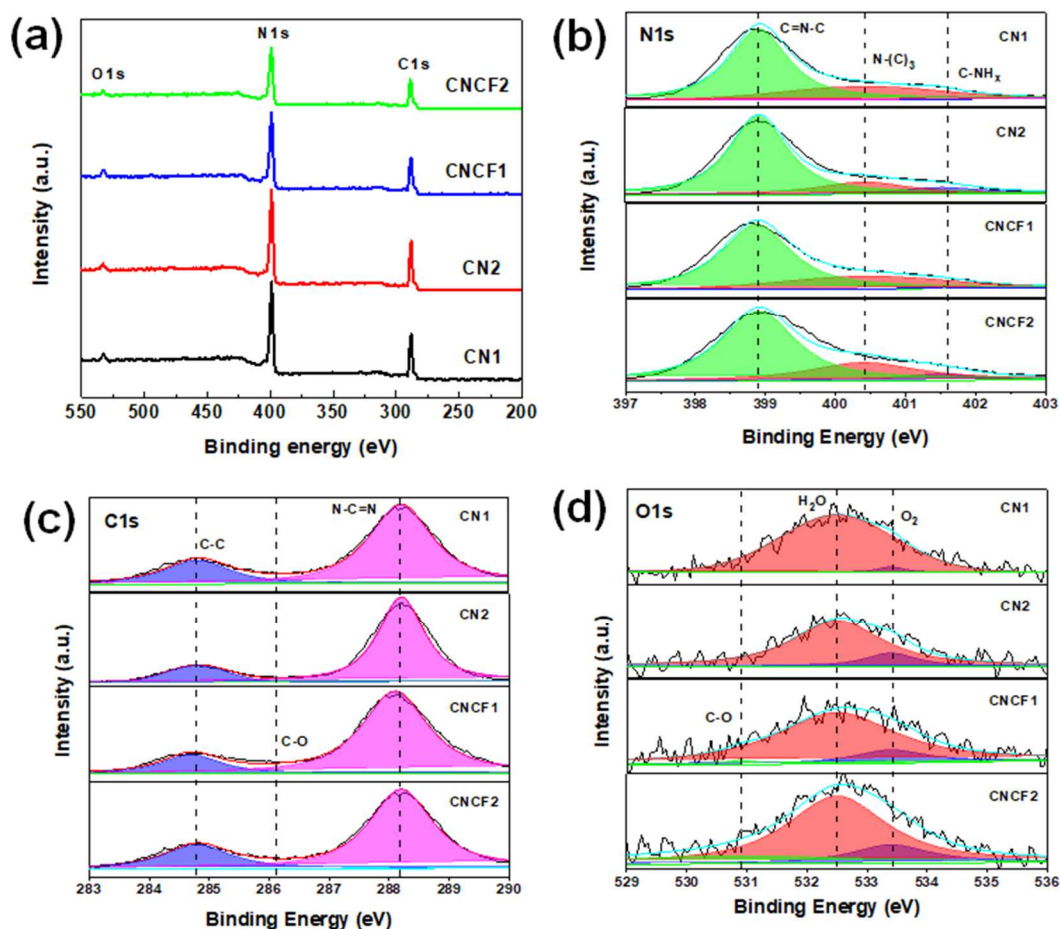
307

308 **Figure 2.** Scanning electron microscopy (SEM) images of CN1 and CNCF1; transmission  
 309 electron microscopy (TEM) and TEM mapping of CNCF1 (a), SEM images of CN2 and CNCF2;  
 310 TEM and TEM mapping of CNCF2 (b).

311

312 Scanning electron microscopy (SEM) and transmission electron microscopy  
 313 (TEM) revealed the morphology and microstructure of CN<sub>x</sub> and CNCF<sub>x</sub> (x = 1 or 2).  
 314 As shown in Figure 2, CN1 and CN2 are mainly composed of stacked irregular  
 315 nanosheets. Compared with CN1, a thinner sheet-like structure was obtained for CN2  
 316 upon calcination. For samples after pyrolysis (CNCF1 and CNCF2), carbon  
 317 nanofibers with an average length of 0.1–1 μm were identified on top of or between  
 318 micron-sized layers of carbon nitride. Sheet-like carbon nitride particles of 8–12 μm

319 width were observed by TEM (Figure 2), suggesting that the assembly also occurs at  
 320 the nanometer scale because isolated carbon nanofibers  $\varnothing \approx 10\text{--}20$  nm were identified.  
 321 This clearly showcases the integration of the CNF within the  $g\text{-C}_3\text{N}_4$  during the  
 322 assembly prior to pyrolysis. Elemental mapping by TEM shows that C and N, the two  
 323 main elements of carbon nitride, are uniformly spread in CNCF1 and CNCF2, and  
 324 only traces of oxygen are likewise distributed (Figure 2).



325  
 326 **Figure 3.** X-ray photoelectron spectroscopy data of CN1, CN2, CNCF1, and CNCF2 samples:  
 327 survey scan (a), core spectra with deconvolution for N1s (b), C1s (c), and O1s (d).

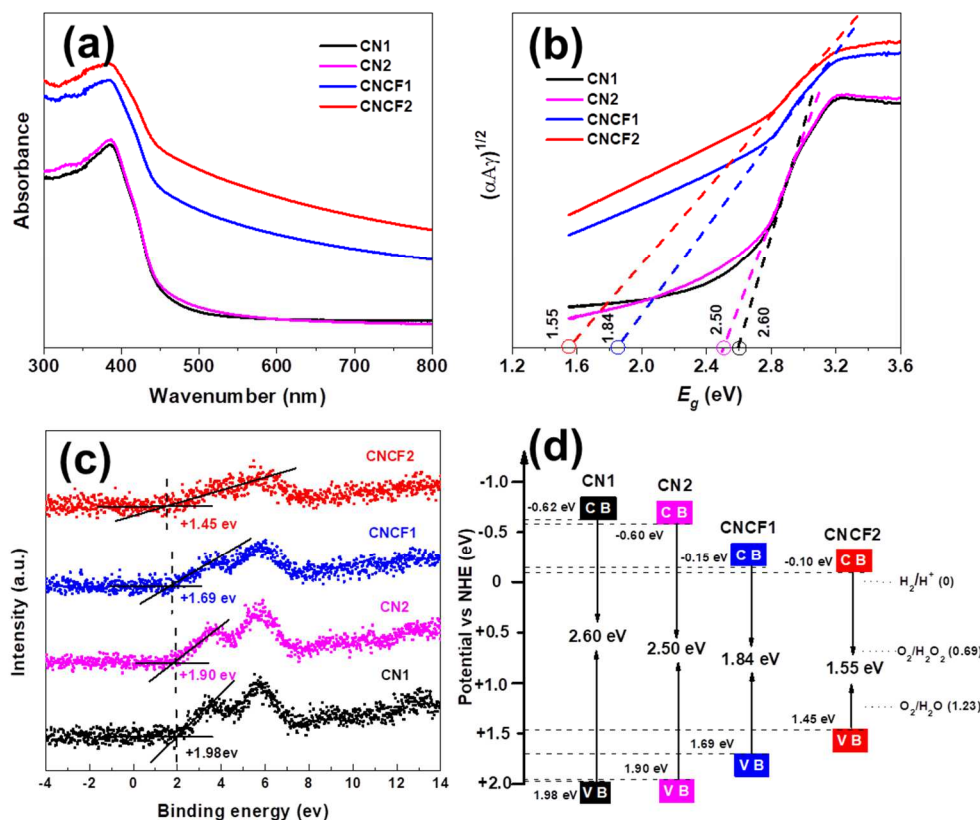
328

329 X-ray photoelectron spectroscopy (XPS) allowed us to identify the composition  
 330 and chemical status of the main elements in the samples (Figure 3). As shown in  
 331 Figure 3a, similar X-ray photoelectron spectra were recorded for the four samples  
 332 exhibiting the two peaks expected for  $g\text{-C}_3\text{N}_4$ , namely N 1s and C 1s and a weak  
 333 signal of O 1s [67]. For N 1s spectra in Figure 3b, the three peaks at 398.9, 400.4, and

334 401.5 eV are assigned to  $sp^2$ -hybridized nitrogen (C=N-C), tertiary nitrogen (N-(C<sub>x</sub>)<sub>3</sub>)  
335 and C-NH<sub>x</sub>, respectively [41]. An estimate of the relative proportion of the different  
336 species was obtained by deconvolution (Table S2). It appears that the percentage of  
337 C-NH<sub>x</sub> either in CN2 or CNCF2 prepared by the bi-component route is considerably  
338 higher than that for the materials prepared by the mono-component route (CN1 and  
339 CNCF1). This is an additional indication of the effect of the urea precursor during the  
340 formation of the materials, and it is consistent with the FT-IR data [68] (Figure 1a).  
341 Moreover, the content of C-NH<sub>x</sub> decreased after g-C<sub>3</sub>N<sub>4</sub> was assembled and pyrolyzed  
342 with CNF, a possible explanation being the reaction of this amino group with the  
343 functional groups of cellulose (hydroxyl and carboxylic group) during assembly or  
344 with gaseous products issued from the decomposition of cellulose during pyrolysis.

345 In Figure 3c, C 1s spectrum could be deconvoluted into two peaks at 284.8 and  
346 288.2 eV. The peak at 288.2 eV represents by far the highest proportion of C species  
347 and was attributed to  $sp^2$ -hybridized carbon covalently bound by N atom (N=C-N), as  
348 expected for g-C<sub>3</sub>N<sub>4</sub>. The peak at 284.8 eV was assigned to C-C carbon species [69],  
349 both routes of preparation led to a similar quantity of this species, indicating the  
350 presence of carbonaceous residue. With the assembly and pyrolysis of CNF, the  
351 content of N-C=N decreased by a few percent and that of C-C increased by 10% for  
352 CNCF1, which is expected because the pyrolysis of CNF leads to the formation of  
353 carbonaceous char that can adsorb on the surface of g-C<sub>3</sub>N<sub>4</sub>. However, this increase  
354 was not observed when comparing CN2 and CNCF2 and is attributable to a higher  
355 integration of the carbon fiber into the sheet-like structure of g-C<sub>3</sub>N<sub>4</sub>. C 1s XPS data  
356 also revealed a peak at 286.1 eV for CNCF1 and CNCF2, which was ascribed to C-O  
357 [70] that likely results from the assembly and pyrolysis with CNF, which generates  
358 O-containing carbon as observed in carbon-derived polysaccharides [71]. However,  
359 different routes of preparation resulted in different C-O content: 1–2% in CNCF1  
360 versus 4–5 % for CNCF2. Concerning oxygen, the high-resolution O 1s spectra was  
361 fitted based on two reference peaks centered at binding energies of 533.4 eV and  
362 532.5 eV for adsorbed O<sub>2</sub> and adsorbed H<sub>2</sub>O, respectively [72]. Compared with the  
363 as-prepared g-C<sub>3</sub>N<sub>4</sub> samples CN1 and CN2, the new peak at 530.9 eV in

364 CNF-modified g-C<sub>3</sub>N<sub>4</sub> samples (CNCF1 and CNCF2) was ascribed to C-O [73].  
 365 These data are consistent with the C-O content observed on the C1 XPS spectra, the  
 366 proportion of O in C-O species being 1–2% in CNCF1 and 3–4 % in CNCF2.

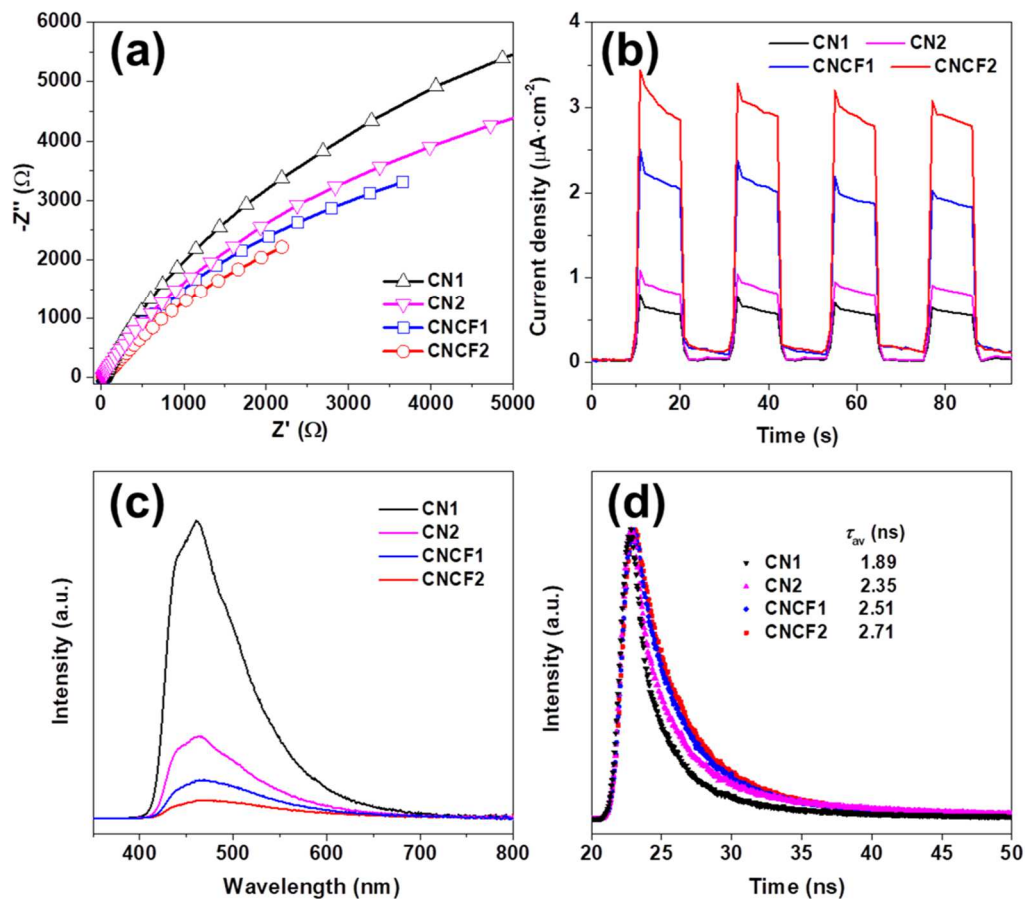


367  
 368 **Figure 4.** For CN1, CN2, CNCF1, and CNCF2: characterization by UV-vis DRS spectra (a),  
 369 determination of the band gaps (b), determination of VB XPS spectra (c), and energy band  
 370 structures (d)

371

372 To investigate the optical absorption and band structures, UV-visible diffuse  
 373 reflectance spectra (UV-vis DRS) of the samples were recorded (Figure 4a). All  
 374 samples presented absorption in the blue region typical of the 2D structure of carbon  
 375 nitride [74]. However, compared with CN1 and CN2, the absorption intensity of both  
 376 CNCF1 and CNCF2 was significantly increased owing to the presence of carbon  
 377 fibers and multiple reflection of incident ray light across porous structures and band  
 378 structure regulation [75]. The corresponding band gaps determined from Tauc's plots  
 379 were 2.60, 2.50, 1.84, and 1.55 eV for CN1, CN2, CNCF1, and CNCF2, respectively

380 (Figure 4b). Therefore, the CNCF1 and CNCF2 samples exhibited a narrower band  
381 gap than other samples and consequently higher absorption of visible light useful in  
382 photogenerating carriers. The band structures of different samples were further  
383 investigated by VB XPS spectra as shown in Figure 4c. An additional effect of the  
384 presence of carbon fibers is the variation of the VB potential; values for CN1 (1.98 eV)  
385 and CN2 (1.90 eV) were decreased for CNCF1 (1.69 eV) and CNCF2 (1.45 eV). A  
386 decrease in the VB potential is beneficial in narrowing the band gap and decreasing  
387 the generation of  $\cdot\text{OH}$  because of the decreased oxidation ability. Combining the VB  
388 XPS spectra (Figure 4c), the location of VB and CB bands was determined using the  
389 formula  $E_g = E_{\text{VB}} - E_{\text{CB}}$  (where  $E_g$ : band gap,  $E_{\text{VB}}$ : VB value,  $E_{\text{CB}}$ : CB value; Figure  
390 4d). The  $E_g$  of CNCF1 and CNCF2 was smaller than that of CN1 and CN2,  
391 respectively. Importantly, the  $E_g$  is the smallest for CNCF2, which also has a more  
392 positive CB level (-0.1 eV vs NHE) than other samples, which is 0.79 eV more  
393 negative than the reduction potential of  $\text{O}_2/\text{H}_2\text{O}_2$  (0.69 eV) and large enough to reduce  
394  $\text{O}_2$  to  $\text{H}_2\text{O}_2$  [76]. Moreover, the positive shift of CB could easily trigger  
395 photogenerated electrons from CB, accepting electrons from carbon fibers and  
396 enhancing the two-electron reduction of  $\text{O}_2$  to  $\text{H}_2\text{O}_2$  [77, 78].



397

398 **Figure 5.** Electrochemical impedance spectra: Nyquist plots (a), transient photocurrent response  
 399 curves (b), photoluminescence spectra (c), time-resolved photoluminescence decay spectra (d) of  
 400 the samples.

401

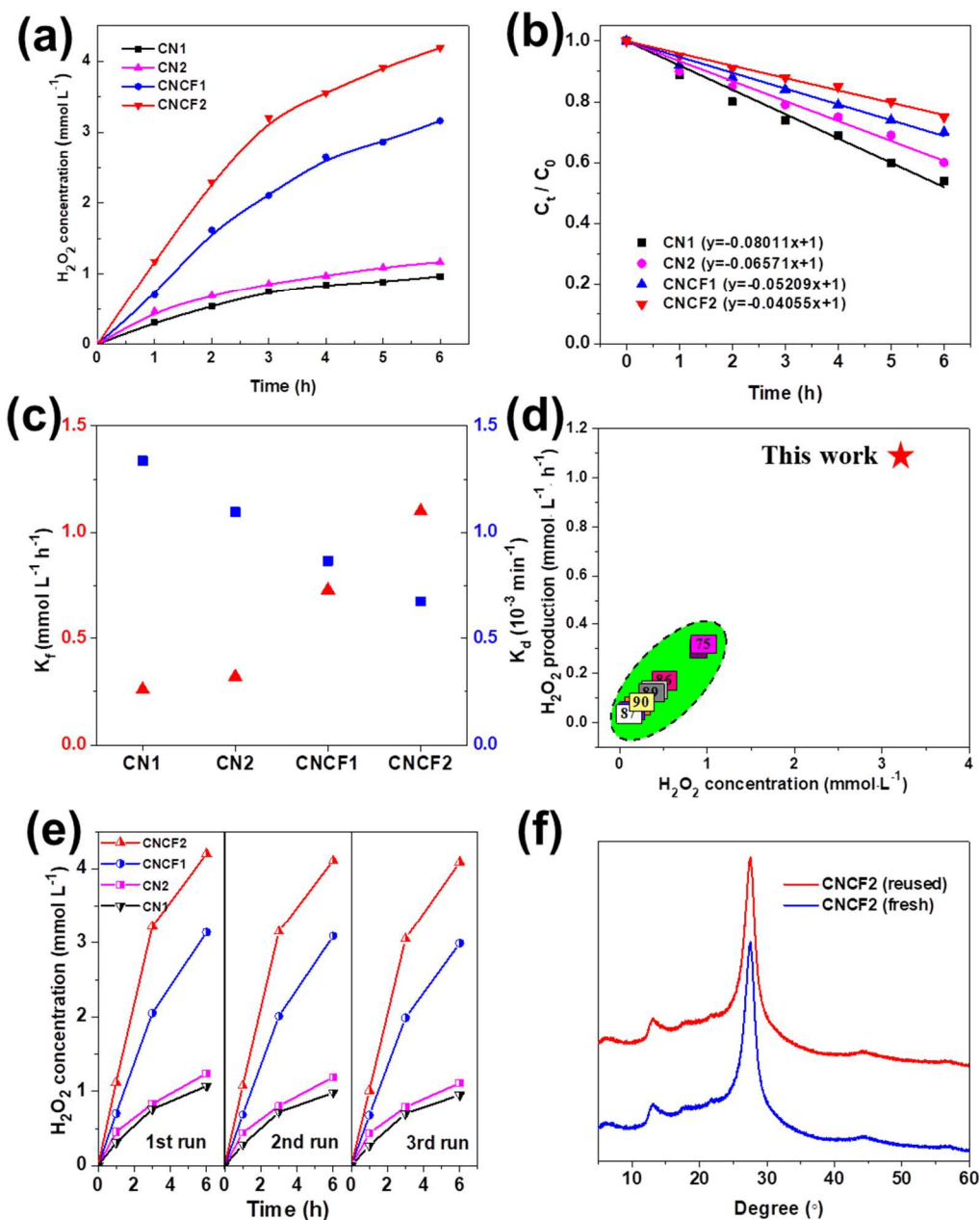
402 Electrochemical impedance spectroscopy (EIS) was further employed to  
 403 understand the charge separation and their transfer. As shown in Figure 5a, the  
 404 Nyquist plots revealed that under visible light irradiation, the observed arc radius of  
 405 CNCF<sub>x</sub> is smaller than the corresponding CN<sub>x</sub>, which indicates that the charge  
 406 transfer resistance of CNCF<sub>x</sub> is significantly decreased. This is ascribed to the  
 407 introduction of carbon nanofibers and carbonaceous residue that enhance electron  
 408 transfer. The smaller arc radius of CNCF2 than CNCF1 indicates a faster charge  
 409 transfer and a better efficiency of electron–hole separation. The transient photocurrent  
 410 curves under visible light irradiation of the as-prepared samples are shown in Figure  
 411 5b. CNCF1 and CNCF2 displayed much higher photocurrent than that of CN1 and  
 412 CN2, confirming that carbon fibers derived from nanocellulose accelerate electron

413 transfer. The recombination/separation of photogenerated species was investigated by  
414 photoluminescence (PL) spectra of the samples (Figure 5c). As a general trend, the  
415 lower the photoluminescence peak intensity, the higher the efficiency of  
416 photogenerated electron-hole pairs. The strong fluorescence emission peaks of CN1  
417 (462 nm) and CN2 (466 nm) were slightly red shifted to 470 nm and 469 nm for  
418 CNCF1 and CNCF2, respectively, which further confirms the band gap decrease [79].  
419 CNCF1 and CNCF2 samples had considerably lower photoluminescence intensities  
420 than CN1 and CN2, respectively, suggesting better separation rate of electrons and  
421 holes. Moreover, it is worth noting that the photoluminescence quenching efficiency  
422 of CNCF2 was lower than CNCF1, suggesting more effective electron transfer from  
423 photogenerated g-C<sub>3</sub>N<sub>4</sub> to nanocarbon fibers [74]. To obtain the average radiative  
424 lifetime of the recombining charge carriers, time-resolved photoluminescence (TRPL)  
425 characterization was investigated (Figure 5d). The average radiative lifetime ( $\tau_{ave}$ ) was  
426 further calculated according to the following equation:  $\tau_{ave} = (B_1\tau_1^2 + B_2\tau_2^2)/(B_1\tau_1 +$   
427  $B_2\tau_2)$ . The value of  $\tau_{ave}$  for CN1 and CN2 was 1.89 and 2.35 ns, respectively, whereas  
428 that for CNCF1 and CNCF2 was 2.51 and 2.71 ns, respectively. This result indicated  
429 that, with the addition of carbon fibers derived from nanocellulose, the markedly  
430 extended lifetime of photogenerated charge carriers accelerates the charge separation  
431 efficiency. In summary, the presence of cellulose-derived carbon fibers assembled  
432 with g-C<sub>3</sub>N<sub>4</sub> highly improved the efficiency of the photocatalysts in promoting charge  
433 transfer and carrier separation in g-C<sub>3</sub>N<sub>4</sub>.

434

435

### 436 **3.2 Photocatalytic production of H<sub>2</sub>O<sub>2</sub>**



437

438 **Figure 6.** Photocatalytic production of H<sub>2</sub>O<sub>2</sub> as a function of time under visible light with CN1,

439 CN2, CNCF1, and CNCF2 as photocatalysts (a); photocatalytic decomposition of H<sub>2</sub>O<sub>2</sub> under

440 visible light irradiation (b); formation rate (K<sub>f</sub>) and decomposition rate constant (K<sub>d</sub>) for H<sub>2</sub>O<sub>2</sub>

441 photocatalytic production (c); comparison of reported photocatalytic performances (photocatalytic

442 production rate of H<sub>2</sub>O<sub>2</sub> within 3h and H<sub>2</sub>O<sub>2</sub> concentration after 3h reaction) (d); reusability

443 assessment of the different photocatalysts (e); X-ray diffraction patterns of CNCF2 before and

444 after photocatalytic H<sub>2</sub>O<sub>2</sub> production (f)

445

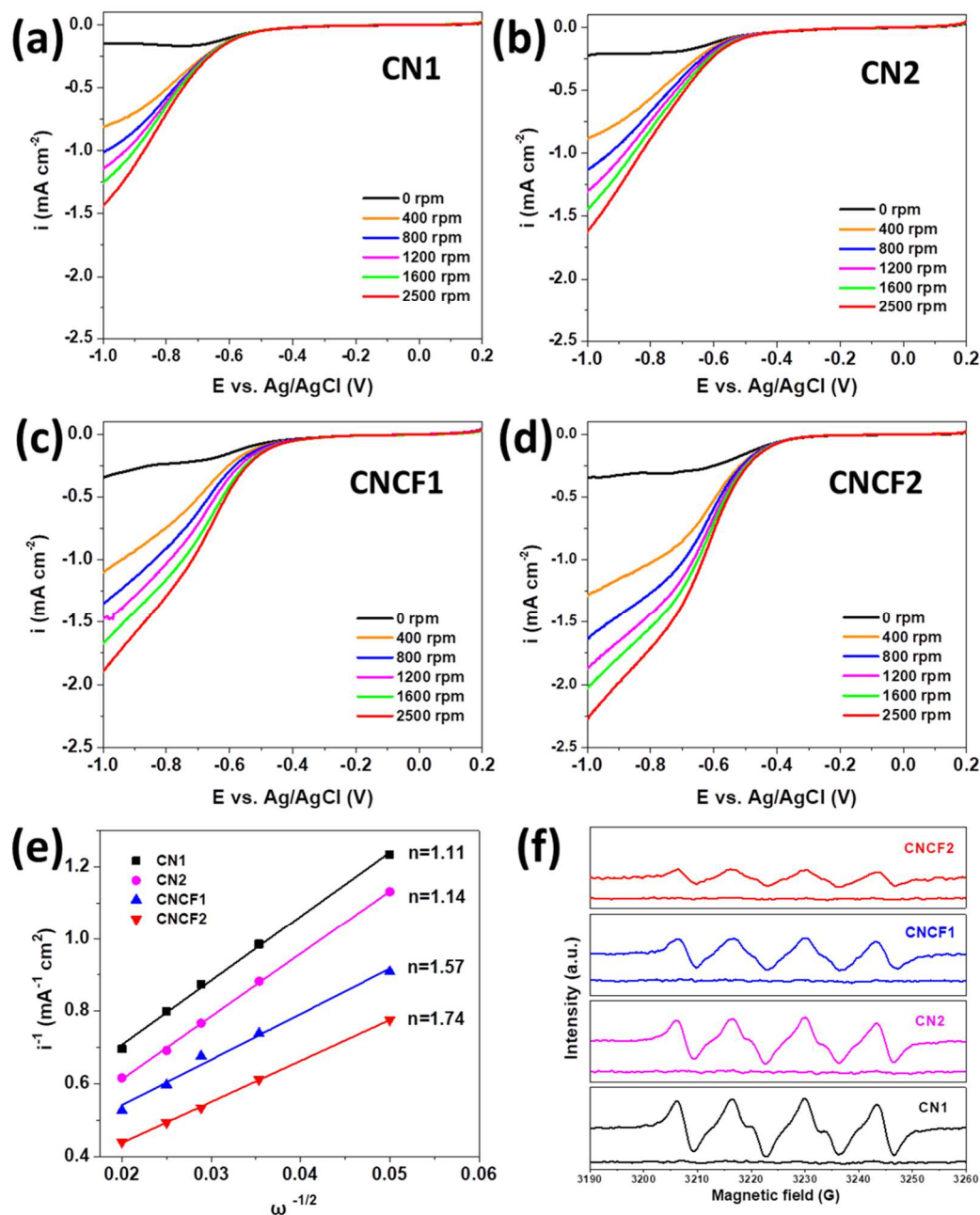
446 Photocatalytic production of H<sub>2</sub>O<sub>2</sub> under visible light irradiation was evaluated  
447 by measuring the quantity of H<sub>2</sub>O<sub>2</sub> versus time of reaction under atmospheric pressure  
448 at 25 ± 0.1°C using a catalyst concentration of 1.00 ± 0.01 g L<sup>-1</sup> (Figure 6a). Because  
449 ethanol is known to have a good effect on photocatalytic H<sub>2</sub>O<sub>2</sub> production when used  
450 as a proton donor (Figure S4), 5 mL (85.9 mmol) ethanol was used in this  
451 photocatalytic system with an ethanol-to-water ratio of 1: 9 (v/v). With CN1, only  
452 0.31 mmol L<sup>-1</sup> of H<sub>2</sub>O<sub>2</sub> is formed after 1 h. Although the productivity is improved  
453 with CN2, it remains low: 0.47 mmol L<sup>-1</sup> of H<sub>2</sub>O<sub>2</sub> after 1 h. CNCF1 and CNCF2  
454 presented a considerably higher H<sub>2</sub>O<sub>2</sub> productivity after 1 h, 0.7 mmol L<sup>-1</sup> and 1.18  
455 mmol L<sup>-1</sup>, respectively. Therefore, the kinetic study presented in Figure 6c suggests  
456 that the order of photocatalytic efficiency is as follows: CNCF2 > CNCF1 > CN2 >  
457 CN1.

458 The decomposition behavior of H<sub>2</sub>O<sub>2</sub> was investigated under visible light  
459 irradiation with photocatalysts and a H<sub>2</sub>O<sub>2</sub> concentration =1 mmol L<sup>-1</sup>. As shown in  
460 Figure 6b, the level of H<sub>2</sub>O<sub>2</sub> decomposition was ~8% and ~5% with CNCF1 and  
461 CNCF2, respectively, after 1 h of visible light irradiation, which was lower than that  
462 with CN1 and CN2 (~10%). The H<sub>2</sub>O<sub>2</sub> decomposition rate constant (K<sub>d</sub>) was  
463 calculated with the following equation:  $K_d = -\ln(C_t/C_0)/t$ , where  $C_t$  is the H<sub>2</sub>O<sub>2</sub>  
464 concentration at time  $t$ , and  $C_0$  is the initial concentration of H<sub>2</sub>O<sub>2</sub> (1 mmol L<sup>-1</sup>).  
465 Figure 6c shows that the K<sub>d</sub> of CN1 ( $1.335 \times 10^{-3} \text{ min}^{-1}$ ) and CN2 ( $1.095 \times 10^{-3} \text{ min}^{-1}$ )  
466 was higher than that of CNCF1 ( $0.868 \times 10^{-3} \text{ min}^{-1}$ ) and CNCF2 ( $0.676 \times 10^{-3} \text{ min}^{-1}$ ).  
467 These results confirm that carbon fibers derived from nanocellulose effectively inhibit  
468 the decomposition of H<sub>2</sub>O<sub>2</sub> on carbon nitride.

469 Compared with previously reported values [7, 75, 80-86], the photocatalyst  
470 CNCF2 presented a significantly improved activity (Figure 6d). To investigate the  
471 recyclability of the as-prepared photocatalysts, after 6 h of reaction time, the catalyst  
472 was separated and washed from the suspension by filtration and then used again in a  
473 new batch of H<sub>2</sub>O<sub>2</sub> production under the same conditions (Figure 6e). After three  
474 cycles, the photocatalyst was almost unchanged and the photocatalytic activity was

475 maintained. The X-ray diffraction analysis showed that both the fresh and reused  
 476 CNCF2 catalysts exhibited almost the same typical peaks, as shown in Figure 6f.

477



478

479 **Figure 7.** Linear sweep voltammetry curves of CN1 (a), CN2 (b), CNCF1 (c) and CNCF2 (d)  
 480 measured on a rotating disk electrode at different rotating speeds; Koutecky-Levich plots of the  
 481 data obtained at a constant electrode potential (-1.0 V vs. Ag/AgCl) (e), Electron paramagnetic  
 482 resonance spectra of the DMPO- $\cdot$ O<sub>2</sub><sup>-</sup> adduct (f)

483

484 To further investigate the O<sub>2</sub> reduction pathway, a rotating disk electrode (RDE)  
485 analysis of the O<sub>2</sub> reduction reaction (ORR) was performed. The linear sweep  
486 voltammetry (LSV) curves in Figure 7a-d for the as-prepared samples were measured  
487 by an RDE in phosphate buffer solution (0.1 mol L<sup>-1</sup>, pH = 7) at different rotating  
488 speeds. The Koutecky-Levich plots derived from the LSV data are presented in Figure  
489 7e. The average number of transfer electrons was calculated using the following  
490 equations:

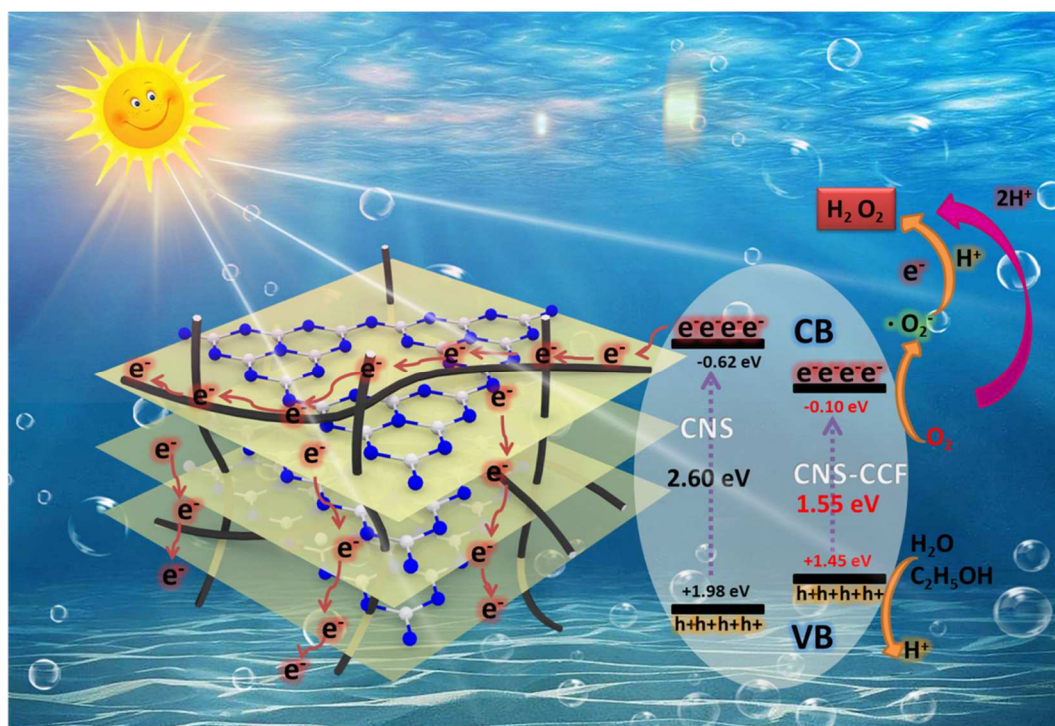
$$j^{-1} = j_k^{-1} + B^{-1}\omega^{-1/2}$$

$$B = 0.2nF\nu^{-1/6}CD^{2/3}$$

493 , where  $j$  is the current density,  $j_k$  is the kinetic current density,  $\omega$  is the rotating speed,  
494  $F$  is the Faraday constant (96485 C mol<sup>-1</sup>),  $\nu$  is the kinetic viscosity of water (0.01 cm<sup>2</sup>  
495 s<sup>-1</sup>), and  $C$  is the O<sub>2</sub> concentration in water (1.26 × 10<sup>-5</sup> mol cm<sup>-3</sup>). The average number  
496 of electrons ( $n$ ) was 1.11 and 1.14 for CN1 and CN2, respectively, and 1.57 and 1.74  
497 for CNCF1 and CNCF2, respectively. These results suggest that single-electron O<sub>2</sub>  
498 reduction occurs on CN1 and CN2 because the  $n$  value of CN1 and CN2 was  
499 approximately 1. In contrast, the average number of electrons is above 1.5 when  
500 nanocellulose-derived carbon is present, especially for CNCF2, for which an O<sub>2</sub>  
501 reduction by two-electron process is likely. Thus, the ORR for CNCF1 and CNCF2  
502 had a hybrid single/two-electron function, whereas that for CN1 and CN2 showed  
503 only single-electron function.

504 Electron paramagnetic resonance (EPR) analysis with DMPO as a trapping agent  
505 of ·O<sub>2</sub><sup>-</sup> was performed to identify the pathway of conversion of molecular oxygen to  
506 H<sub>2</sub>O<sub>2</sub>. As shown in Figure 7f, the characteristic peaks of DMPO·O<sub>2</sub><sup>-</sup> were observed in  
507 all samples, indicating that ·O<sub>2</sub><sup>-</sup> was generated as an intermediate in the formation of  
508 H<sub>2</sub>O<sub>2</sub>. As seen in Figure 7f, CN1 and CN2 both presented higher-intensity EPR  
509 signals than CNCF1 and CNCF2, indicating that CN1 and CN2 generate more ·O<sub>2</sub><sup>-</sup>  
510 than CNCF1 and CNCF2. The finding implies that reduction of O<sub>2</sub> into ·O<sub>2</sub><sup>-</sup> occurs on  
511 the four samples by a single-electron pathway leading to H<sub>2</sub>O<sub>2</sub> formation. It is  
512 interesting that, CNCF1 and CNCF2 present partial O<sub>2</sub> directly reduction into H<sub>2</sub>O<sub>2</sub>  
513 by a two-electron pathway[87]. Scheme 2 illustrates photocatalytic H<sub>2</sub>O<sub>2</sub> production

514 by nanocellulose-derived C/g-C<sub>3</sub>N<sub>4</sub> nano-heterojunction. Cellulose nanofibers with  
 515 -OH and -COOH groups can bind to carbon nitride with intrinsic amino groups (-NH,  
 516 -NH<sub>2</sub>) and thermally transform into an effective heterojunction, increasing the linking  
 517 between g-C<sub>3</sub>N<sub>4</sub> nanosheets and carbon fibers. Furthermore, the carbon fibers reduce  
 518 the band gap and greatly increase the electron transfer during the photocatalytic  
 519 reaction. The photocatalytic efficiency also depends on the capacity and strength of  
 520 adsorption of molecular oxygen onto the surface of carbon nitride. By porosimetric,  
 521 BET SSA of CN2 is 2.2 times higher than that of CN1 (Table S1), which provides  
 522 more space and active sites to adsorb oxygen molecules [88]. The adsorption strength  
 523 of molecular oxygen is also potentially reinforced by the presence of N atoms of  
 524 amino groups in CN2, which are able to bind to oxygen as a Lewis acid [89]. As  
 525 previously reported, such adsorption of oxygen on the surface of the photocatalyst  
 526 catalyst is highly beneficial to the electron transfer [90]. An exciting point is to  
 527 observe that with the presence of carbon nanofiber, the EPR intensity of  $\cdot\text{O}_2^-$   
 528 CNCF1 is higher than CNCF2. The data demonstrate the interest of the bi-component  
 529 synthetic route chosen for the preparation of the g-C<sub>3</sub>N<sub>4</sub>. This is ascribed to both the  
 530 larger BET specific surface area and the specific photophysical properties.



531

532 **Scheme 2.** Role of cellulosic carbon fibers for photocatalytic H<sub>2</sub>O<sub>2</sub> production photocatalyzed by  
533 a nanocellulose-derived carbon/g-C<sub>3</sub>N<sub>4</sub> nanocomposite.

534

#### 535 **4. Conclusions**

536 The high improvement of the photocatalytic production of hydrogen peroxide  
537 (H<sub>2</sub>O<sub>2</sub>) over carbon nitride (g-C<sub>3</sub>N<sub>4</sub>) that we report is ascribable of main major  
538 phenomenon. First, we show that the presence of a very low content of  
539 nanocellulose-derived carbon deeply modify the photoactivity of the g-C<sub>3</sub>N<sub>4</sub>  
540 assembled with it. The result is an outstanding photocatalytic H<sub>2</sub>O<sub>2</sub> production of 1.10  
541 mmol L<sup>-1</sup> h<sup>-1</sup> under visible light. The second critical point is to achieve a high level of  
542 interaction between the g-C<sub>3</sub>N<sub>4</sub> nanosheets and CNF when assembling these two  
543 nanocomponents. Third, a high level of interaction can be achieved through the  
544 preparation of amino-rich g-C<sub>3</sub>N<sub>4</sub> using a bi-component mixture of melamine and  
545 urea. When carbon fibers are closely incorporated into the stacked structure of g-C<sub>3</sub>N<sub>4</sub>,  
546 the nanofibers not only improve the porosity of the materials but also have a strong  
547 effect on the photophysical properties of the g-C<sub>3</sub>N<sub>4</sub> in narrowing the band gap;  
548 improving the visible light absorption; increasing the number of photogenerated  
549 carriers, especially excitable electrons; and accelerating the electron transfer and  
550 further promoting a direct two-electron O<sub>2</sub> reduction reaction to generate hydrogen  
551 peroxide. In subsequent studies, this approach will be tested for other materials for the  
552 photoproduction of other chemicals.

553

#### 554 **Acknowledgments**

555 This work was supported by the Project Funded by China Postdoctoral Science  
556 Foundation (2020T130215), Key Laboratory of State Forestry and Grassland Ministry  
557 (2019KFJJ16), Distinguished Young Talents of Fujian Agriculture and Forestry  
558 University (XJQ201806), Science and Technology Innovation Fund of Fujian  
559 Agriculture and Forestry University (CXZX2018013), and Fujian Innovation and  
560 Entrepreneurship Training Program (S202010389078).

561

562 **References**

- 563 [1] W.C. Hou, Y.S. Wang, *ACS Sustainable Chemistry & Engineering* 5 (2017) 2994-3001.
- 564 [2] H. Hou, X. Zeng, X. Zhang, *Angewandte Chemie-International Edition* 59 (2019)  
565 17356-17376.
- 566 [3] Y. Yang, R.Z. Dong, Y.L. Zhu, H.S. Li, H. Zhang, X.M. Fan, H.L. Chang, *Chemical*  
567 *Engineering Journal* 381 (2020) 122749.
- 568 [4] T. Kato, K. Yoshizawa, *European Journal of Organic Chemistry* 2011 (2011) 4113-4120.
- 569 [5] Y. Sun, L. Silvioli, N.R. Sahraie, W. Ju, J. Li, A. Zitolo, S. Li, A. Bagger, L. Arnarson, X.  
570 Wang, T. Moeller, D. Bernsmeier, J. Rossmesl, F. Jaouen, P. Strasser, *Journal of the*  
571 *American Chemical Society* 141 (2019) 12372-12381.
- 572 [6] H. Hirakawa, S. Shiota, Y. Shiraishi, H. Sakamoto, S. Ichikawa, T. Hirai, *ACS Catalysis* 6  
573 (2016) 4976-4982.
- 574 [7] S. Kim, G.-h. Moon, H. Kim, Y. Mun, P. Zhang, J. Lee, W. Choi, *Journal of Catalysis* 357  
575 (2018) 51-58.
- 576 [8] L. Yang, G. Dong, D.L. Jacobs, Y. Wang, L. Zang, C. Wang, *Journal of Catalysis* 352 (2017)  
577 274-281.
- 578 [9] C. Kormann, D.W. Bahnemann, M.R. Hoffmann, *Environmental Science & Technology* 22  
579 (1988) 798-806.
- 580 [10] D. Tsukamoto, A. Shiro, Y. Shiraishi, Y. Sugano, S. Ichikawa, S. Tanaka, T. Hirai, *ACS*  
581 *Catalysis* 2 (2012) 599-603.
- 582 [11] T. Hirakawa, Y. Nosaka, *The Journal of Physical Chemistry C* 112 (2008) 15818-15823.
- 583 [12] M. Teranishi, S. Naya, H. Tada, *Journal of the American Chemical Society* 132 (2010)  
584 7850-7851.
- 585 [13] H. Goto, Y. Hanada, T. Ohno, M. Matsumura, *Journal of Catalysis* 225 (2004) 223-229.
- 586 [14] L. Zheng, J. Zhang, Y.H. Hu, M. Long, *The Journal of Physical Chemistry C* 123 (2019)  
587 13693-13701.
- 588 [15] S. Sun, X. Yu, Q. Yang, Z. Yang, S. Liang, *Nanoscale Advances* 1 (2019) 34-63.
- 589 [16] C. Ray, T. Pal, *Journal of Materials Chemistry A* 5 (2017) 9465-9487.
- 590 [17] Z. Haider, H.I. Cho, G.H. Moon, H.I. Kim, *Catalysis Today* 335 (2019) 55-64.
- 591 [18] Z. Li, N. Xiong, G. Gu, *Dalton Transactions* 48 (2019) 182-189.

- 592 [19] X. Li, J. Zhang, F. Zhou, H. Zhang, J. Bai, Y. Wang, H. Wang, Chinese Journal of Catalysis  
593 39 (2018) 1090-1098.
- 594 [20] G.F. Zuo, S.S. Liu, L. Wang, H. Song, P.X. Zong, W.S. Hou, B.D. Li, Z.L. Guo, X.G. Meng,  
595 Y. Du, T. Wang, V.A.L. Roy, Catalysis Communication 123 (2019) 69-72.
- 596 [21] A. Thomas, A. Fischer, F. Goettmann, M. Antonietti, J.O. Muller, R. Schlogl, J.M. Carlsson,  
597 Journal of Materials Chemistry 18 (2008) 4893-4908.
- 598 [22] S. Samanta, R. Yadav, A. Kumar, A.K. Sinha, R. Srivastava, Applied Catalysis  
599 B-Environmental 259 (2019) 118054.
- 600 [23] H. Wang, Y.H. Guan, S.Z. Hu, Y.B. Pei, W.T. Ma, Z.P. Fan, Nano 14 (2019) 1950023.
- 601 [24] J. Tian, T.J. Wu, D. Wang, Y. Pei, M.H. Qiao, B.N. Zong, Catalysis Today 330 (2019)  
602 171-178.
- 603 [25] X.Y. Qu, S.Z. Hu, P. Li, Z. Li, H. Wang, H.F. Ma, W. Li, Diamond and Related Materials 86  
604 (2018) 159-166.
- 605 [26] L.H. Zheng, J.Z. Zhang, Y.H. Hu, M.C. Long, Journal of Physical Chemistry C 123 (2019)  
606 13693-13701.
- 607 [27] S.Z. Hu, X.Y. Qu, P. Li, F. Wang, Q. Li, L.J. Song, Y.F. Zhao, X.X. Kang, Chemical  
608 Engineering Journal 334 (2018) 410-418.
- 609 [28] H.L. Tian, H.Q. Fan, J.W. Ma, L.T. Ma, G.Z. Dong, Electrochim Acta 247 (2017) 787-794.
- 610 [29] Y.J. Zhou, L. Li, Y.H. Wan, T.T. Chen, X. Chu, Analytic Methods 10 (2018) 5084-5090.
- 611 [30] W. Liu, J.B. Zhou, Z.S. Hu, Separation Purification Technology 227 (2019) 115665.
- 612 [31] Y.K. Wang, S.Z. Hu, Q. Li, G.Z. Gu, Y.F. Zhao, H.Y. Liang, W. Li, RSC Advances 8 (2018)  
613 36903-36909.
- 614 [32] S. Asadzadeh-Khaneghah, A. Habibi-Yangjeh, K. Nakata, Journal of Photochemistry and  
615 Photobiology A-Chemistry 374 (2019) 161-172.
- 616 [33] D.L. Jiang, Y. Zhang, H.Y. Chu, J. Liu, J. Wan, M. Chen, RSC Advances 4 (2014)  
617 16163-16171.
- 618 [34] S. Zhao, T. Guo, X. Li, T.G. Xu, B. Yang, X. Zhao, Applied Catalysis B-Environmental 224  
619 (2018) 725-732.
- 620 [35] M.L. Foresti, A. Vázquez, B. Boury, Carbohydrate Polymers 157 (2017) 447-467.
- 621 [36] T. Dou, L. Zang, Y. Zhang, Z. Sun, L. Sun, C. Wang, Materials Letters 244 (2019) 151-154.

- 622 [37] H. Wang, J. Li, N. Ding, X. Zeng, X. Tang, Y. Sun, T. Lei, L. Lin, *Chemical Engineering*  
623 *Journal* 386 (2020) 124021.
- 624 [38] P. Yang, J. Wang, G. Yue, R. Yang, P. Zhao, L. Yang, X. Zhao, D. Astruc, *Journal of*  
625 *Photochemistry and Photobiology A: Chemistry* 388 (2019) 112169.
- 626 [39] W. Bai, X. Yang, X. Du, Z. Qian, Y. Zhang, L. Liu, J. Yao, *Applied Surface Science* 504  
627 (2020) 144179.
- 628 [40] H. Zhao, S. Chen, X. Quan, H. Yu, H. Zhao, *Applied Catalysis B: Environmental* 194 (2016)  
629 134-140.
- 630 [41] H. Qi, X. Ji, C. Shi, R. Ma, Z. Huang, M. Guo, J. Li, Z. Guo, *Journal of Colloid Interface*  
631 *Science* 556 (2019) 366-375.
- 632 [42] X. Li, X. Qian, X. An, J. Huang, *Applied Surface Science* 487 (2019) 1262-1270.
- 633 [43] S. Chen, W. Lu, J. Han, H. Zhong, T. Xu, G. Wang, W. Chen, *Chemical Engineering Journal*  
634 359 (2019) 119-129.
- 635 [44] S. Wang, F. Li, X. Dai, C. Wang, X. Lv, G.I.N. Waterhouse, H. Fan, S. Ai, *Journal of*  
636 *Hazardous Materials* 384 (2020) 121417.
- 637 [45] F. Li, Z. Yu, H. Shi, Q. Yang, Q. Chen, Y. Pan, G. Zeng, L. Yan, *Chemical Engineering*  
638 *Journal* 322 (2017) 33-45.
- 639 [46] S.-W. Zhao, M. Zheng, H.-L. Sun, S.-J. Li, Q.-J. Pan, Y.-R. Guo, *Dalton Transactions* (2019)  
640 3723-3734.
- 641 [47] B. Wu, L. Ge, H. Wu, X. Wang, Q. Ge, J. Miao, M. Cao, P. Chen, R. Xia, J. Qian, *Advanced*  
642 *Materials Interfaces* 6 (2019) 1801406.
- 643 [48] L. Mu, L. Shi, Y. Wang, Q. Zhou, J. Ye, X. Feng, *Journal of Materials Chemistry C* 6 (2018)  
644 12660-12667.
- 645 [49] W.S. Lin, W. Hong, L. Sun, D. Yu, D.S. Yu, X.D. Chen, *Chemsuschem* 11 (2018) 114-119.
- 646 [50] Z. Jin, J. Chen, S. Huang, J. Wu, Q. Zhang, W. Zhang, Y.-J. Zeng, S. Ruan, T. Ohno,  
647 *Catalysis Today* 315 (2018) 149-154.
- 648 [51] Y. Li, R. Jin, Y. Xing, J. Li, S. Song, X. Liu, M. Li, R. Jin, *Advanced Energy Materials* 6  
649 (2016) 1601273.
- 650 [52] L. Liu, W. Sun, W. Yang, Q. Li, J.K. Shang, *Scientific Reports* 6 (2016) 20878.

651 [53] F. Dong, Z. Zhao, T. Xiong, Z. Ni, W. Zhang, Y. Sun, W.-K. Ho, ACS Applied Materials &  
652 Interfaces 5 (2013) 11392-11401.

653 [54] F. Dong, Z. Ni, P. Li, Z. Wu, New Journal of Chemistry 39 (2015) 4737-4744.

654 [55] S. Martha, A. Nashim, K.M. Parida, Journal of Materials Chemistry A 1 (2013) 7816-7824.

655 [56] D.M. Ruan, S. Kim, M. Fujitsuka, T. Majima, Applied Catalysis B-Environmental 238 (2018)  
656 638-646.

657 [57] J. Tian, D. Wang, S. Li, Y. Pei, M. Qao, Z.-H. Li, J. Zhang, B. Zong, ACS Sustainable  
658 Chemistry & Engineering 8 (2020) 594-603.

659 [58] Y.L. Li, P.P. Li, J.S. Wang, Y.L. Yang, W.Q. Yao, Z. Wei, J.S. Wu, X.X. Yan, X.F. Xu, Y.H.  
660 Liu, Y.F. Zhu, Applied Catalysis B-Environmental 225 (2018) 519-529.

661 [59] F. Dong, Z.Y. Wang, Y.J. Sun, W.K. Ho, H.D. Zhang, Journal of Colloid Interface Science  
662 401 (2013) 70-79.

663 [60] H. Yu, R. Shi, Y. Zhao, T. Bian, Y. Zhao, C. Zhou, G.I.N. Waterhouse, L.Z. Wu, C.H. Tung, T.  
664 Zhang, Advanced Materials 29 (2017) 1605148.

665 [61] A.J. Cai, Q. Wang, Y.F. Chang, X.P. Wang, Journal of Alloys and Compounds 692 (2017)  
666 183-189.

667 [62] Y. Yang, C. Zhang, D. Huang, G. Zeng, J. Huang, C. Lai, C. Zhou, W. Wang, H. Guo, W. Xue,  
668 R. Deng, M. Cheng, W. Xiong, Applied Catalysis B: Environmental 245 (2019) 87-99.

669 [63] J.S. Zhang, Y. Chen, X.C. Wang, Energy & Environmental Science 8 (2015) 3092-3108.

670 [64] P. Niu, H. Li, Y. Ma, T. Zhai, The Journal of Physical Chemistry C 122 (2018) 20717-20726.

671 [65] J. Xu, L. Zhang, R. Shi, Y. Zhu, Journal of Materials Chemistry A 1 (2013) 14766-14772.

672 [66] F. Dong, Z.W. Zhao, T. Xiong, Z.L. Ni, W.D. Zhang, Y.J. Sun, W.K. Ho, ACS Applied  
673 Materials Interfaces 5 (2013) 11392-11401.

674 [67] H.J. Li, B.W. Sun, L. Sui, D.J. Qian, M. Chen, Physical Chemistry Chemical Physics 17  
675 (2015) 3309-3315.

676 [68] J. Zhang, F. Huang, Applied Surface Science 358 (2015) 287-295.

677 [69] L. Shi, L. Yang, W. Zhou, Y. Liu, L. Yin, X. Hai, H. Song, J. Ye, Small 14 (2018) 1703142.

678 [70] J.X. Huang, D.G. Li, R.B. Li, Q.X. Zhang, T.S. Chen, H.J. Liu, Y. Liu, W.Y. Lv, G.G. Liu,  
679 Chemical Engineering Journal 374 (2019) 242-253.

680 [71] P. Deng, H. Li, Z. Wang, Y. Hou, Applied Surface Science 504 (2020) 144454.

681 [72] F. Cheng, J. Yan, C. Zhou, B. Chen, P. Li, Z. Chen, X. Dong, *Journal of Colloid Interface*  
682 *Science* 468 (2016) 103-109.

683 [73] A. Sánchez-Sánchez, F. Suárez-García, A. Martínez-Alonso, J.M.D. Tascón, *Carbon* 70 (2014)  
684 119-129.

685 [74] G. Wang, Y. Zhao, H. Ma, C. Zhang, X. Dong, X. Zhang. *Science of The Total Environment*  
686 756 (2020) 144139.

687 [75] R. Wang, X. Zhang, F. Li, D. Cao, M. Pu, D. Han, J. Yang, X. Xiang, *Journal of Energy*  
688 *Chemistry* 27 (2018) 343-350.

689 [76] S. Zhao, X. Zhao, S. Ouyang, Y. Zhu, *Catalysis Science & Technology* 8 (2018) 1686-1695.

690 [77] D. Tsukamoto, A. Shiro, Y. Shiraishi, Y. Sugano, S. Ichikawa, S. Tanaka, T. Hirai, *ACS*  
691 *Catalysis* 2 (2012) 599-603.

692 [78] Y. Shiraishi, S. Kanazawa, Y. Kofuji, H. Sakamoto, S. Ichikawa, S. Tanaka, T. Hirai,  
693 *Angewandte Chemie International Edition* 53 (2014) 13454-13459.

694 [79] J.L. Yuan, X. Liu, Y.H. Tang, Y.X. Zeng, L.L. Wang, S.Q. Zhang, T. Cai, Y.T. Liu, S.L. Luo, Y.  
695 Pei, C.B. Liu, *Applied Catalysis B-Environmental* 237 (2018) 24-31.

696 [80] G. Zuo, S. Liu, L. Wang, H. Song, P. Zong, W. Hou, B. Li, Z. Guo, X. Meng, Y. Du, T. Wang,  
697 V.A.L. Roy, *Catalysis Communications* 123 (2019) 69-72.

698 [81] Y. Kofuji, S. Ohkita, Y. Shiraishi, H. Sakamoto, S. Tanaka, S. Ichikawa, T. Hirai, *ACS*  
699 *Catalysis* 6 (2016) 7021-7029.

700 [82] Z. Zhu, H. Pan, M. Murugananthan, J. Gong, Y. Zhang, *Applied Catalysis B-Environmental*  
701 232 (2018) 19-25.

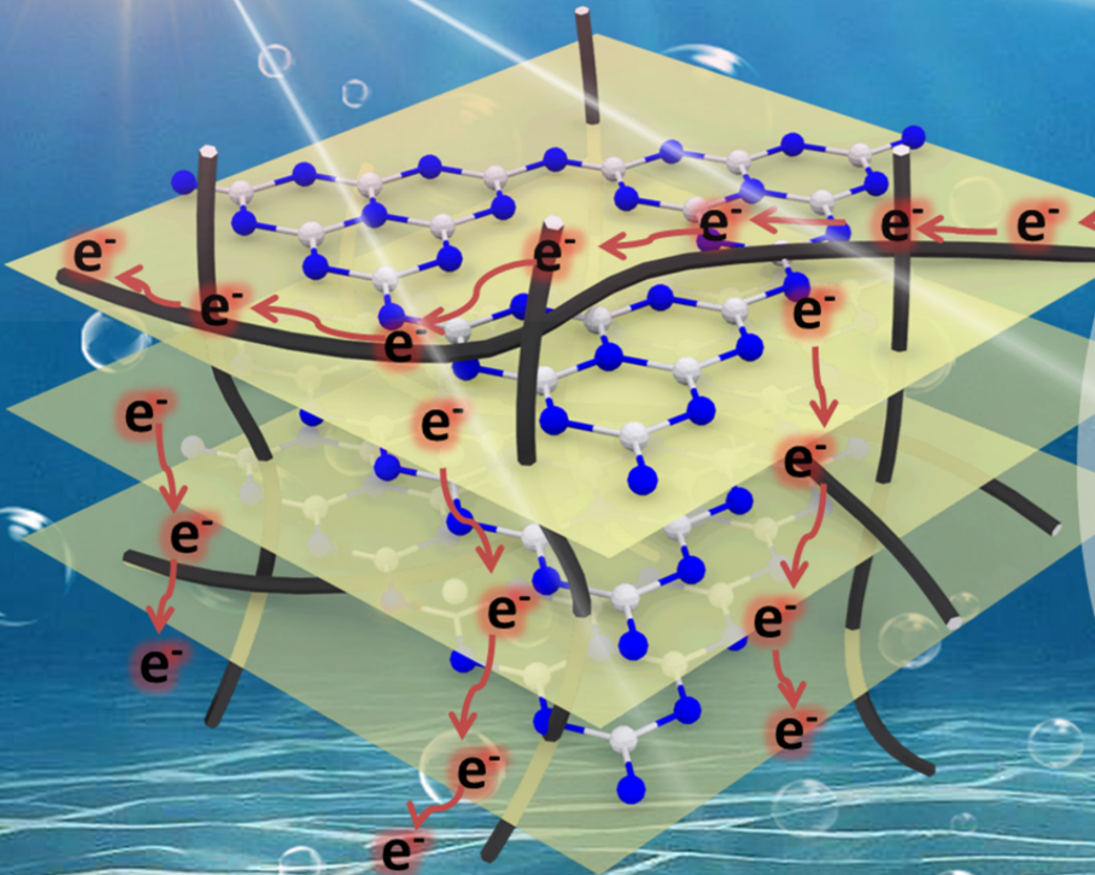
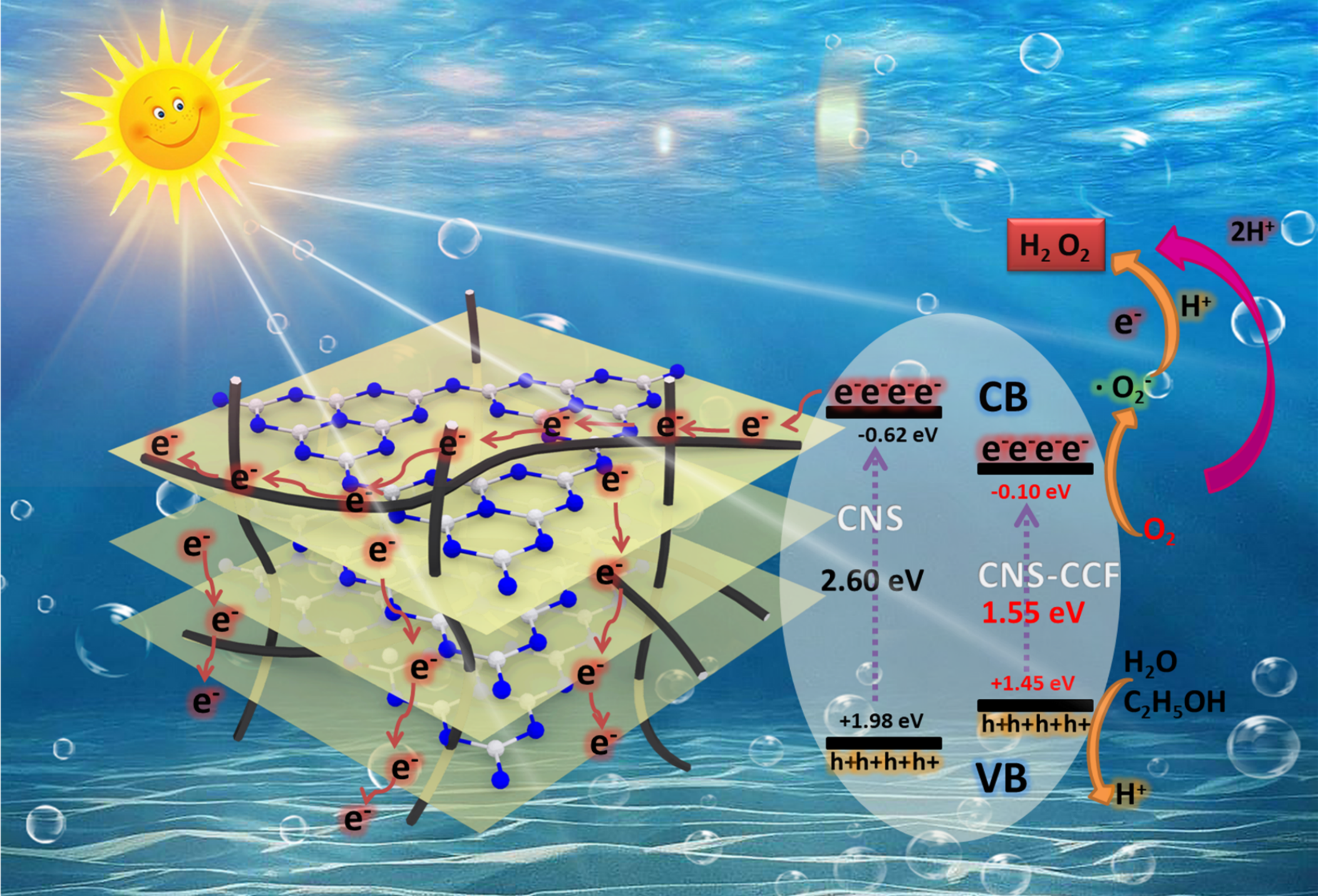
702 [83] S. Zhao, X. Zhao, H. Zhang, J. Li, Y. Zhu, *Nano Energy* 35 (2017) 405-414.

703 [84] Y. Yang, Z. Zeng, G. Zeng, D. Huang, R. Xiao, C. Zhang, C. Zhou, W. Xiong, W. Wang, M.  
704 Cheng, W. Xue, H. Guo, X. Tang, D. He, *Applied Catalysis B: Environmental* 258 (2019)  
705 117956.

706 [85] Z. Wei, M. Liu, Z. Zhang, W. Yao, H. Tan, Y. Zhu, *Energy & Environmental Science* 11  
707 (2018) 2581-2589.

708 [86] G.-h. Moon, M. Fujitsuka, S. Kim, T. Majima, X. Wang, W. Choi, *ACS Catalysis* 7 (2017)  
709 2886-2895.

- 710 [87] S. Zhao, T. Guo, X. Li, T. Xu, B. Yang, X. Zhao, *Applied Catalysis B-Environmental* 224  
711 (2018) 725-732.
- 712 [88] X. Li, J. Zhang, F. Zhou, H. Zhang, J. Bai, Y. Wang, H. Wang, *Chinese Journal of Catalysis*  
713 39 (2018) 1090-1098.
- 714 [89] S. Li, G. Dong, R. Hailili, L. Yang, Y. Li, F. Wang, Y. Zeng, C. Wang, *Applied Catalysis*  
715 *B-Environmental* 190 (2016) 26-35.
- 716 [90] J. Goclon, K. Winkler, *Applied Surface Science* 462 (2018) 134-141.
- 717



$e^-e^-e^-e^-$   
-0.62 eV

CNS

2.60 eV

+1.98 eV  
 $h+h+h+h+$

CB  
 $e^-e^-e^-e^-$

-0.10 eV

CNS-CCF  
1.55 eV

+1.45 eV  
 $h+h+h+h+$

VB

